ADVANCED ELECTRONIC MATERIALS Open Access
www.advelectronicmat.de

Ultrafast Dynamics of Electronic and Structural Modifications Induced by Photoexcitation in Cerium Oxide

*Samuele Pelatti, Eleonora Spurio, Daniele Catone, Patrick O'Keeffe, Stefano Turchini, Giuseppe Ammirati, Fulvio Paleari, Daniele Varsano, Stefania Benedetti, Alessandro di Bona, Sergio D'Addato, Yifeng Jiang, Peter Zalden, Yohei Uemura, Hao Wang, Doriana Vinci, Xinchao Huang, Frederico Lima, Mykola Biednov, Dmitry Khakhulin, Christopher Jackson Milne, Federico Boscherini, and Paola Luches**

Pump-probe spectroscopies utilizing X-ray free-electron lasers offer element-specific insights into the processes occurring in photocatalysts following photoexcitation, which are essential for the rational optimization of the efficiency of these materials. This study examines the dynamic evolution of the electronic and atomic structure in stoichiometric cerium oxide films following photoexcitation, employing ultrafast pump-probe X-ray absorption spectroscopy (XAS) at the Ce L_3 edge in both the near-edge and extended energy ranges using an X-ray free electron laser. The results reveal a rapid relaxation pathway occurring within the first few hundred femtoseconds, followed by the formation of an excited state with a lifetime on the order of hundreds of picoseconds. The analysis of pump-probe XAS in the extended energy range identifies a structural distortion consistent with the formation of a photoinduced small polaron state. The observed time correlation between the photoinduced electronic and structural changes further reinforces the hypothesis of photoinduced polaron formation. Constrained density functional theory simulations offer insights into the electronic modifications and structural distortions in the photoexcited material. The consequences of the observed processes on material functionality are discussed.

1. Introduction

The performance of photocatalytic materials strongly depends on the processes occurring after photoexcitation. A thorough understanding of the decay pathways of photoexcited charge carriers within the host material can help explain the observed increase in activity induced by light absorption and guide the development of strategies to optimize conversion efficiency. Indeed, photoexcited charge carriers often experience ultrafast recombination or become trapped in band-gap states, which limit their mobility and reduce the probability of reaching the surface to participate in chemical reactions.[1] The band-gap states can arise from extrinsic factors, such as defect sites like oxygen vacancies, impurities, or low-coordination sites, or from intrinsic characteristics of the material.[2] In particular, the interaction

S. Pelatti, E. Spurio, S. D'Addato
Dipartimento di Fisica Informatica e Matematica
Università di Modena e Reggio Emilia
Via G. Campi 213/a, Modena 41121, Italy

S. Pelatti, E. Spurio, F. Paleari, D. Varsano, S. Benedetti, A. di Bona, S. D'Addato, P. Luches
CNR – Istituto Nanoscienze
Via G. Campi 213/a, Modena 41121, Italy
E-mail: paola.luches@nano.cnr.it

The ORCID identification number(s) for the author(s) of this article can be found under https://doi.org/10.1002/aelm.202500429

DOI: 10.1002/aelm.202500429

D. Catone, S. Turchini, G. Ammirati
EuroFEL Support Laboratory (EFSL)
CNR – Istituto di Struttura della Materia
Rome 00133, Italy

P. O'Keeffe
EuroFEL Support Laboratory (EFSL)
CNR – Istituto di Struttura della Materia
Monterotondo Scalo 00015, Italy

Y. Jiang, P. Zalden, Y. Uemura, H. Wang, D. Vinci, X. Huang, F. Lima, M. Biednov, D. Khakhulin, C. J. Milne
European XFEL
Holzkoppel 4, 22869 Schenefeld, Germany

F. Boscherini
CNR – Istituto Officina dei Materiali (IOM)
AREA Science Park – Basovizza, S.S. 14 km 163.5, Trieste 34149, Italy

between photoexcited charge carriers and lattice induces a distortion, which in turn generates a potential that self-traps the excited charges. The quasiparticle associated with the charge-lattice interaction is called a polaron. Polaron formation in the ground state, arising from the incorporation of additional electronic charges into the lattice, is frequently observed in many oxides. In these materials, the interaction between the added charge and the associated lattice distortion limits mobility by confining carriers in band-gap polaronic states.[3] The resulting effective electron mass is increased by the interaction, and electrical conduction occurs solely through thermally induced hopping of trapped charge carriers. In analogy, the formation of polarons after photoexcitation has been identified as a key factor limiting the photoactivity of compounds such as hematite[4,5] and other oxides. On the other hand, extrinsic polaronic states originating from defects can broaden the absorption range of oxides, decrease the recombination rate, and enhance photoactivity.[6,7]

In cerium oxide, a material widely used as a catalyst or photocatalyst,[8–10] the localization of extra charges in 4f states significantly limits the electron-based conductivity, which occurs through polaron hopping.[11] Theoretical calculations have shown that polaron formation leads to an expansion of the Ce—O bond length by ≈0.1 Å.[12,13] A study on cerium oxide by some of the authors has provided results compatible with the formation of photoinduced small polarons following band-gap excitation, based on the observed dynamic shift of optical femtosecond transient absorption spectroscopy (FTAS) features within a few hundred femtoseconds.[14] Such charge localization is expected to have a positive impact on cerium oxide-based photocatalysts by weakening the bond between the cation and oxygen, thereby reducing the energy required for oxygen vacancy formation, which is crucial for the material's functionality. At the same time, it can extend the lifetime of the photoexcited carriers.

However, FTAS lacks elemental and structural sensitivity, which limits its ability to provide a clear and unique picture of the underlying processes. Extreme ultra-violet and X-ray-based ultrafast spectroscopies have been demonstrated to be able to provide very detailed information on the dynamics of photoexcitation and decay processes in various materials.[15–20] Specifically, for hematite, small polaron formation after photoexcitation was inferred from the observed sub-100 fs splitting of the Fe $M_{2,3}$ edge.[15] The characteristic formation times, energies, and the dependence of the formation rate on the excitation wavelength were also evaluated.[15] A study on WO_3 has found evidence for a metastable state associated with a structural change that forms within a few hundred picoseconds.[16,17] A recent investigation suggests a rapid electron polaron formation within 0.7 ps, followed by fast decay into deep trapping states within less than 10 ps in a cerium oxide single crystal.[18]

The present study correlates the dynamics of the evolution of the Ce-related electronic structure, obtained through pump-probe X-ray absorption near-edge spectroscopy (XANES), with the evolution of the local atomic structure around Ce ions, analyzed via pump-probe extended-range X-ray absorption fine structure (EXAFS) at the Ce L_3 edge. The research takes advantage of the capabilities of X-ray free electron lasers, unique facilities that provide ultrashort, high intensity coherent X-ray pulses, tunable in energy, that can be synchronized with ultrashort optical laser pulses with variable delay.[21] In particular, the FXE instrument

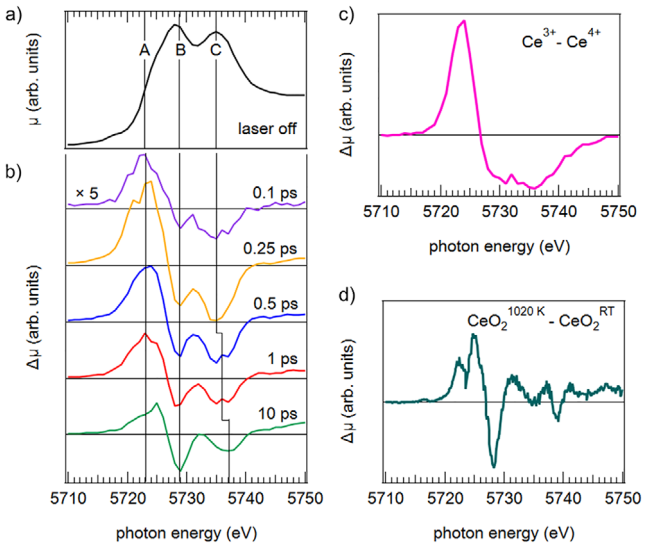

Figure 1. Ce L_3-edge XANES: a) steady-state spectrum; b) transient spectra at different delay times; c) difference between spectra measured on Ce^{3+} and Ce^{4+} reference samples; d) difference between two steady–state Ce L_3-edge HERFD-XANES spectra measured at 1020 K and at RT (from reference 41).

at the European X-ray Free Electron Laser (Eu-XFEL) facility,[22] allows pump-probe XANES and EXAFS on thin films to be measured with high counting rates. The data clearly demonstrate the formation of photoinduced small polarons in cerium oxide, providing information on formation time, on the associated structural distortions, and on the modifications of the electronic structure. Constrained density functional theory (DFT) calculations modelling an excited electron-hole pair, with the electron localized on the Ce f-band, support the experimental interpretation.

2. Results

2.1. XANES

XANES analyzes the absorption of X-rays near the absorption edge, enabling direct determination of electronic structure of specific elements.

Figure 1a shows the steady–state Ce L_3-edge XANES spectrum of the cerium oxide film acquired before excitation. The shape is consistent with that observed for compounds in which Ce atoms are in the 4+ oxidation state,[23] as expected for the cerium oxide film investigated in this study (see also XPS and UV–vis absorptance spectra, and the XRD pattern shown in the Figures S1-S3, Supporting Information). The spectrum shows a main edge at 5723 eV (A) and two post-edge features attributed to transitions to the 5d e_g and t_{2g} crystal-field split levels in two configurations, one with a screened core hole (B) and the other with an unscreened core hole (C).[24]

To gain insight into the dynamic evolution of the electronic structure in photoexcited cerium oxide, we performed pump-probe Ce L_3-edge XANES measurements on the CeO_2 film at various delay times following photoexcitation. Figure 1b shows the transient spectra $\Delta\mu = \mu_{ON} - \mu_{OFF}$, where μ_{ON} and μ_{OFF} are the absorption spectra measured with and without laser

excitation, respectively. The transient spectra at positive delay times display three main features: a positive peak at 5723 eV, close to the main edge (A), and two negative features at energies close to the two maxima (B and C) of the steady-state Ce L_3 XANES in Figure 1a. The A feature is also very close in energy to the Ce L_3 XANES white line maximum in Ce^{3+}-containing compounds (see Figure S4, Supporting Information). A subtle, yet discernible, transient spectrum is detected at a delay time of 0.1 ps (spectrum multiplied by 5 in Figure 1b). As the delay time increases to 0.25 ps, the transient spectrum exhibits a marked increase in the intensity of both positive and negative features. As the delay time is further increased up to 10 ps, the overall intensity of the pump-probe signal gradually decreases, accompanied by detectable changes in the spectral shape. Specifically, the negative peak B at 5729 eV gradually gains a higher relative intensity compared to the other two features, while the second negative feature, C, shifts to higher photon energy, moving from 5735 eV at 0.25 ps to 5737 eV at 10 ps (see also Figures S5 and S6, Supporting Information).

Deriving information about the absorption spectrum of the excited phase μ_{EXC} from the pump-probe XANES transient spectra is not straightforward. Since the laser excites only a fraction of the sample, denoted by α, which is generally unknown and varies with the delay time, the absorption spectrum measured after excitation, μ_{ON}, is given by $\mu_{ON} = \alpha\mu_{EXC} + (1-\alpha)\mu_{OFF}$, where μ_{OFF} is the steady-state spectrum. The transient spectrum, given by:

$$\Delta\mu = \alpha\,\mu_{EXC} + (1-\alpha)\,\mu_{OFF} - \mu_{OFF} = \alpha\left(\mu_{EXC} - \mu_{OFF}\right) \quad (1)$$

is not only proportional to μ_{EXC} but also to μ_{OFF}. It is possible to obtain some qualitative information on μ_{EXC} by comparing the shape of the XANES transient spectra with the difference between spectra measured on Ce^{3+} ($Ce(NO_3)_3$-$6H_2O$) and Ce^{4+} (CeO_2) reference samples – (Figure 1c; Figure S4, Supporting Information), assuming as a first approximation that the primary effect of photoexcitation is the promotion of an electron from the valence band to the Ce 4f levels and the effect of the valence band hole and of the structural rearrangements can be less relevant. At ultrashort delay times of 0.1 and 0.25 ps the transient spectra in Figure 1b show similarities to the Ce^{3+}-Ce^{4+} difference spectrum measured on reference samples reported in Figure 1c, in both the position and branching ratios of the features. This means that at the shortest delay times investigated, the excited state XANES mimics the Ce^{3+} state, with a main edge shifted to lower photon energies and no additional multiplet components.[23,25] However, the two negative features appear significantly narrower in the transient spectra, compared to those in the reference Ce^{3+}-Ce^{4+} difference spectrum, and the C feature progressively shifts to higher photon energies with increasing delay times. The acquired spectra can also be compared with the spectrum shown in Figure 1d, which was obtained from the high-energy resolution fluorescence detected (HERFD) XANES data published in reference [26] by subtracting the steady-state spectrum of a CeO_2 film acquired at room temperature (RT) from a spectrum acquired at 1020 K. The difference spectrum of Figure 1d shows well-resolved fine structure in the A, B and C features. It is however evident that the negative B feature has a higher relative weight than in the Ce^{3+}-Ce^{4+} difference. Moreover, the C feature appears shifted toward higher photon energies, in analogy with the behavior of the transient spectra at 10 ps delay time. The observed behavior of the transient spectra thus suggests that the excited phase can be described as a mixture of a Ce^{3+}-like configuration and a Ce^{4+}-like configuration that has a broadened XANES spectrum, due to lattice thermal effects. At ultrashort delay times of 0.1 ps the Ce^{3+}-like phase dominates, which is consistent with the hypothesis that a few hundreds of fs after photoexcitation the electronic structure of Ce ions closely resembles that of a Ce^{3+} ion. At higher delay times the electronic and the crystalline structure undergo gradual relaxation. The modification of the crystal field strength in the final state, due to electronic and structural rearrangements caused by the hole in the valence band and by the extra electron in the 4f levels, can be responsible for the observed narrowing of transient features B and C and for the progressive shift of feature C. Some modifications related to lattice thermal effects can also contribute at delay times higher than 1 ps.

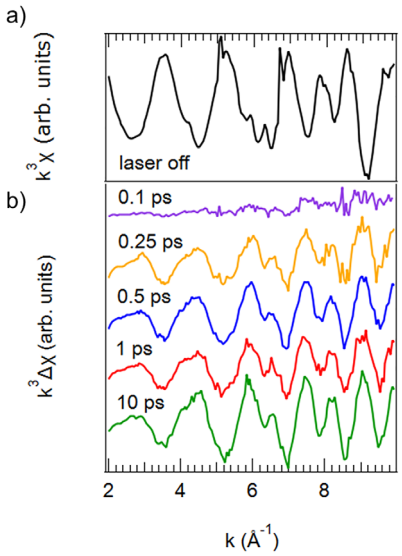

Figure 2. Ce L_3 – edge EXAFS spectra: a) steady-state k^3-weighted $\chi(k)$; b) transient k^3-weighted $\Delta\chi(k)$ at different delay times.

2.2. EXAFS

To go beyond the qualitative picture based on the analysis of pump-probe XANES, pump-probe X-ray absorption over an extended energy range (5700–6100 eV) were measured and quantitatively analyzed, obtaining insights into the transient modifications of the local atomic structure induced in the surroundings of photoexcited Ce ions.

Figure 2a shows the Ce L_3-edge k^3-weighted $\chi(k)$ acquired on the cerium oxide film before excitation, while Figure 2 b reports the transient k^3-weighted $\chi(k)$ at the same delay times used for the transient XANES spectra (the transient spectra $\Delta\mu(E)$ are reported in Figure S7, Supporting Information). The transient EXAFS signal exhibits very low intensity at 0.1 ps. At higher delay times the transient spectra show marked oscillations across the entire k range investigated. The shape of the oscillations does not vary with delay time, likely because the time resolution is insufficient to capture the dynamic evolution of structural distortions.

However, the amplitude of the transient EXAFS signal increases slightly, possibly because a larger fraction of the sample undergoes distortion with increasing delay time.

To proceed with the quantitative analysis of the transient EXAFS data, instead of attempting to extract the excited phase absorption coefficient – which strongly depends on the value of the excited fraction, that is both unknown and possibly variable with delay time – we followed a strategy outlined earlier.[27] In this approach, the transient EXAFS signal is fitted to determine the structural configuration of the excited phase. As shown by the results of the DFT calculations described in the following section, photoexcitation is expected to induce mainly modifications of the local structure of the first coordination shell, to which we limited the analysis. The first shell contribution to the experimental $\Delta\chi(k)$ was obtained by applying the Fourier transform to the data and back-transforming to k space only the first peak in R space (see Figure S8, Supporting Information). In analogy with the $\Delta\mu$ in the XANES region, also the $\Delta\chi^{1st}(k)$ can be expressed as:

$$\Delta\chi^{1st}(k) = \alpha\left(\chi^{1st}_{EXC} - \chi^{1st}_{OFF}\right) \quad (2)$$

where α is the fraction of sample excited by the pump, χ^{1st}_{EXC} is the first shell EXAFS signal of the excited phase and χ^{1st}_{OFF} is the first shell EXAFS signal of the steady-state spectrum acquired before excitation. $\Delta\chi^{1st}(k)$ at the different delay times was fitted with simulated $\Delta\chi$ spectra using FEFFIT.[28] In $\chi^{1st}_{OFF,}$ we included the scattering path that resulted from the first shell fit of the steady-state EXAFS signal of the CeO_2 film, in which the many body amplitude reduction factor S_0^2, the energy origin E_0, the modification of the interatomic Ce—O distance dr and the Debye-Waller factor σ were left as free fitting parameters (see Figure S9, Supporting Information). To obtain a reasonable fit of $\Delta\chi^{1st}(k)$ it was necessary to include two inequivalent scattering paths with the same weight for χ^{1st}_{EXC}, one with a Ce—O distance expanded by dr_{EXC} and one with a Ce—O distance contracted by the same amount. The magnitude of the pump-induced expansion/contraction, dr_{EXC} and the excited fraction α, were treated as free fitting parameters. In χ^{1st}_{EXC}, the parameters S_0^2, E_0, and σ were fixed to the values obtained from fitting the steady-state spectrum, assuming as a first approximation that their value does not change significantly after excitation. A high-quality fit was achieved by assigning equal weight to the two scattering paths that contribute to χ^{1st}_{EXC}. This result can be explained by noting that for each Ce atom excited by the pump – which causes an expansion of the eight O atoms in its first shell – some of the neighboring Ce atoms in the second coordination shell experience a corresponding contraction in the distance to some of the O atoms in their own first shell (see Figure S10, Supporting Information). This simplified model captures the dominant structural changes experienced by the cerium atoms after photoexcitation. The magnitude and the imaginary part of the Fourier transforms of $\Delta\chi^{1st}(k)$ at the different delay times and the resulting fits, as described above, are shown in **Figure 3**. The values of α and of dr_{EXC} obtained from the fit are reported in **Table 1**. The average value of α is ≈4%, within the error bar, consistent with the calculation based on the photon density, sample thickness, and optical absorption coefficient (see also Supporting Information). The scattered values of alpha are due to the strong correlation between the fitting variables. The values of the Ce—O interatomic distance obtained from the fit are in good agreement with the expansion predicted for static polaronic distortions in the literature.[12,13] These distances remain largely unchanged above 0.25 ps, consistent with the formation of a photoinduced polaronic state that expands the first coordination shell of photoexcited Ce atoms and persists throughout the measured delay time range. It was not possible to evaluate the potential contribution of thermal effects to the transient EXFAS spectra at higher delay times. A pump-induced thermal increase would contribute with an increased Debye-Waller factor in the fit of χ^{1st}_{EXC}. Unfortunately, a reliable estimation of σ from the fits of the data at increasing delay times was not possible, due to a high correlation with the α parameter. On the other hand, the negligible variation of the fitted α and dr_{EXC} values over the explored delay time range confirms that thermal effects are not significant and polaronic distortions are the dominant contribution to the transient EXAFS spectra.

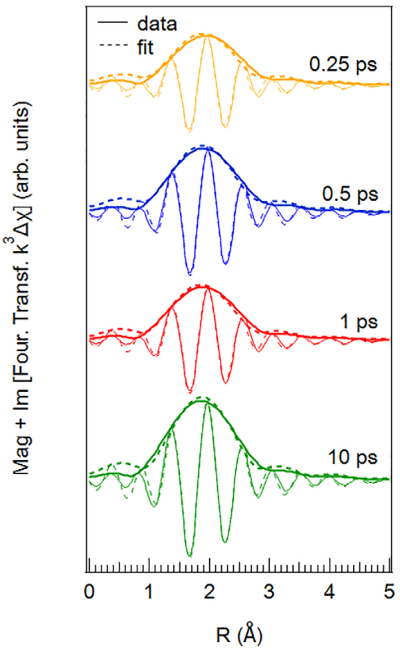

Figure 3. Magnitude and imaginary part of the Fourier transform of the transient k^3-weighted first-shell $\Delta\chi^{1st}(k)$ (solid lines) and fits (dashed lines) at different delay times.

Table 1. Parameters obtained from the first-shell fitting of Ce L_3 edge EXAFS pump-probe difference spectra at the different delay times Δt: α excited fraction, dr_{EXC} change in the Ce—O distance.

Δt [ps]	α [%]	dr_{exc} [Å]
0.25	5 ± 1	0.12 ± 0.01
0.5	4 ± 2	0.14 ± 0.01
1	3 ± 1	0.15 ± 0.02
10	6 ± 2	0.14 ± 0.01

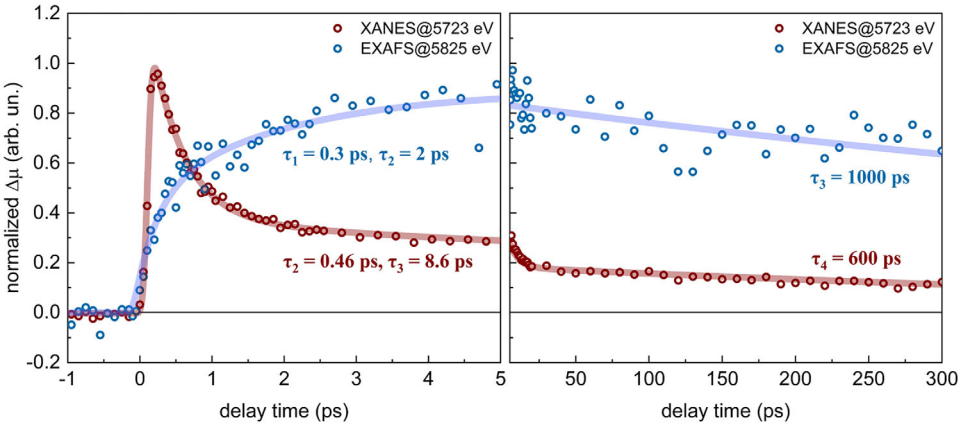

Figure 4. Kinetic traces of the Ce L_3 edge transient signal in the XANES region at hν = 5723 eV (red dots) and in the EXAFS region at hν = 5825 eV (k = 5.2 Å^{-1}) (blue dots), in the 0–5 ps (left panel) and in the 5–300 ps (right panel) delay time interval. The signals have been normalized to have a maximum at 1, for visual comparison. The exponential fits of the signals are also shown as solid lines.

2.3. Kinetics

To gain deeper insight into the origin of the modifications observed upon photoexcitation, we investigated the time evolution of the transient signals in both the XANES and EXAFS regions, which reflect photoinduced changes in the electronic and local atomic structure, respectively. **Figure 4** displays the kinetic traces of the normalized transient signal in two different delay time intervals at two distinct photon energies: 5723 eV, corresponding to the maximum of the transient A feature in the XANES region (see Figure 1), and 5825 eV, corresponding to the second negative peak of $\Delta\chi$ at k = 5.2 Å^{-1} in the EXAFS region (see Figure 2). A fit of the kinetic traces using exponential functions (see Supporting Information) was performed to determine the time constants of the rising and decay dynamics. The transient signal in the XANES region initially rises with a time constant consistent with the instrument response function (IRF) of 50 fs, followed by an exponential decay with an initial characteristic time τ_2 = 0.46 ps, an intermediate decay time τ_3 = 8.6 ps and a slower decay time τ_4 = 600 ps. The transient signal in the EXAFS region rises with an initial characteristic time of τ_1 = 0.3 ps, followed by an intermediate time τ_2 = 2 ps, and by a longer time τ_3 = 1000 ps. The initial rise time of the transient signal in the XANES region corresponds to the photoexcitation of the Ce^{3+}-like phase, before any structural rearrangement. The fast decay time (τ_2 = 0.46 ps) in the XANES region aligns reasonably well with the fast rise time of the transient EXAFS signal obtained from the fit (τ_1 = 0.3 ps), suggesting a time correlation between the observed modifications in the electronic and local atomic structures. This evidence strongly supports the hypothesis of photoinduced polaron formation, wherein the excited charge is stabilized by coupling to the lattice distortion it induces. The intermediate decay times of the transient signals in the XANES region and the intermediate rise time of the transient signal in the EXAFS region can be interpreted as arising from partial evolution of the spectral features related to the electronic and structural changes that lead to polaron formation. At delay times of hundreds of ps the transient signals in the XANES and EXAFS regions, shown in Figure 4, exhibit only a slight decrease, indicating that the material can sustain photoexcited polarons with lifetimes exceeding 300 ps.

2.4. DFT Simulations

To substantiate our experimental findings, we have performed constrained DFT simulations of CeO_2 hosting an excited electron-hole pair. The excited electron occupies the Ce 4f band, while the hole resides within the O 2p valence band (a Hubbard-U correction of 3 eV was employed to properly describe the localization of the f-bands on the Ce atomic sites)[29,30]. A detailed analysis of the electronic structures and geometries of pristine and distorted systems can be found in the Supporting Information (Figures S11–S13, Supporting Information). Our results confirm the formation of a polaronic state via lattice distortion induced by the localization of the excited electron on a Ce atom – which acquires Ce^{3+} spin-polarized character – as can be seen in **Figure 5**a,b depicting the spin-polarized band structure and density of states, respectively. The polaron binding energy (defined as the energy difference between the polaron level and the minimum of the unoccupied Ce^{4+} f-band) is 0.57 eV, in very good agreement with existing computational literature[12,31–34] and in qualitative agreement with the shift we observed experimentally by FTAS.[14] The calculated real-space distribution of the electronic density in the case of the occupied, localized Ce^{3+} polaronic level and unoccupied, delocalized Ce^{4+} band is shown in Figure 5c. The Ce—O bond elongation amounts to 3.45%, corresponding to a calculated dr_{EXC} ≈0.08 Å, in fair agreement with the experimental values obtained from the fits of the pump-probe EXAFS spectra. We find that the presence of the hole, which remains completely delocalized mostly on the oxygen atoms, has a negligible effect, only causing a spin-polarized splitting by ≈50 meV of the topmost valence band and almost no difference in the structural distortion.

3. Discussion

The present work provides strong evidence for photoinduced polaron formation in cerium oxide and enables the determination of the associated electronic and structural modifications. Pump-probe XANES reveals that photoexcitation initially induces the formation of a Ce^{3+}-like state, with a main edge shifted to lower photon energies, without the appearance of additional multiplet

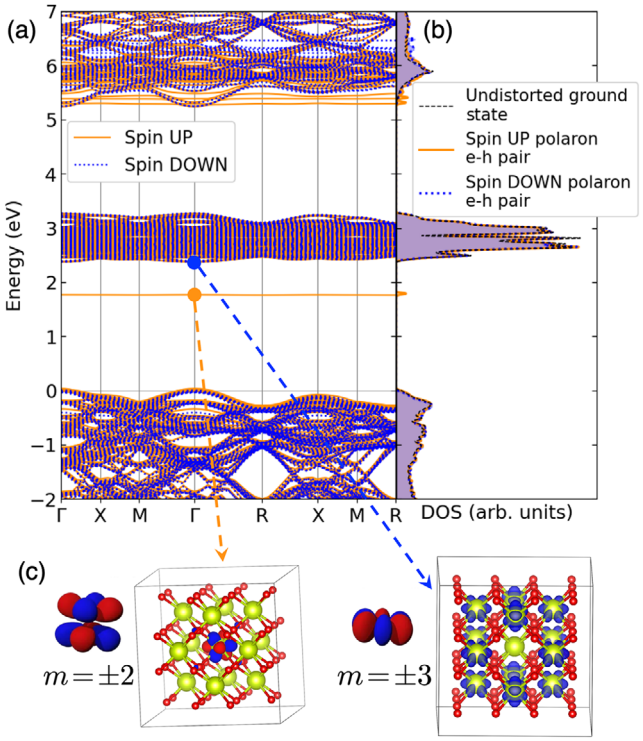

Figure 5. a) Calculated constrained DFT+U band structure of CeO_2 hosting an electron-hole pair (orange: spin-up, blue: spin-down). The polaronic Ce^{3+} level is 0.57 eV below the unoccupied f-band. b) Calculated spin-polarized density of states of the distorted CeO_2 structure (the dashed black line corresponds to the undistorted unconstrained structure). c) Left: real-space representation of the electronic wave function for the Ce^{3+} polaronic level, showing strong electronic localization (corresponding to a f atomic orbital with m = ±2). Right: Real-space representation of the electronic density from the bottom of the unoccupied f band, which is delocalized on top of the remaining Ce^{4+} atoms (corresponding to f atomic orbitals with m = ±3). Here, Ce atoms are displayed in yellow and O atoms in red.

components. Initially, an electron is excited into the Ce 4f level before any further atomic or electronic structural modifications occur. The Ce^{3+}-like state relaxes within ≈0.5 ps to a different excited state in which the electronic structure reflects changes in the local atomic environment of the surrounding O atoms, i.e., a photoinduced small polaron state. The possibility of acquiring high-quality pump-probe EXAFS spectra has also enabled a direct measurement of the structural distortions in an energy region in which the spectra are unaffected by the modifications of the electronic structure. The analysis of the EXAFS data allowed us to identify an expansion of the Ce—O bonds following photoexcitation. The observed structural modification is consistent not only with the expansion theoretically predicted for static polaron formation,[12,13] where an extra charge is added to the material, but also with the expansion that results from the simulations here reported in the case of photoexcited cerium oxide in which a hole in the valence band is also considered. Notably, the observed time correlation between electronic and structural modifications strongly supports the hypothesis of photoinduced polaron formation. The characteristic formation time of the photoinduced polaron, on the order of a few hundred femtoseconds, and its lifetime, exceeding 300 ps, are consistent with our estimates from optical pump-probe spectroscopy on the same system.[14] The formation time of photoinduced polarons has also been investigated in some other materials, finding comparable characteristic times to those observed here.[5,35]

The present study aims to assess the properties of photoinduced polarons in the bulk of a cerium oxide film and is expected to provide a basis for understanding the modifications that may occur at the surface. While the photochemical functionality of a material is determined by its surface properties, a deep understanding of the bulk is required to correctly assess and describe the surface characteristics that are altered by interaction with the environment. A recent work by Katoch et al. investigated a single crystal and a nanocrystalline cerium oxide sample by pump-probe Ce M_5-edge XANES.[18] The observed dynamic changes of the electronic structure in the work by Katoch et al. differ in some respects from those reported in the present work. Specifically, they observed a Ce^{3+}-related signal emerging within ≈0.3 ps and decaying within less than 10 ps, along with a polaron-related signal appearing within ≈0.7 ps and decaying over 10 ps. Our study finds a similar sub-ps polaron formation time, but the photoinduced electronic and structural modifications in our samples persist above 300 ps. It is important to note that the Ce M_5-edge XANES measurements in total electron yield detection mode used by Katoch et al. [18] have a significantly smaller probing depth compared to the Ce L_3-edge XANES measurements in total fluorescence yield detection mode described here. The time required for polaron decay by trapping states can vary significantly between the surface and the bulk of a sample. Additionally, polaron lifetime can be strongly influenced by defect density. In fact, the samples investigated by Katoch et al., show a high defect density in the surface region, as indicated by the pronounced Ce^{3+} contribution in the steady-state XANES spectra,[18] which is not observed in our sample. The much longer photoinduced polaron lifetime observed in our study is likely due to the smaller defect concentration in the probed region our sample. Notably, achieving long-lived excited states is a crucial factor for enhancing the photoinduced functionality of the material. Indeed, the formation energy of oxygen vacancies—key to the functionality of the material—is expected to be transiently reduced in the presence of photoexcited electrons occupying the 4f levels. Photoinduced polaron states with lifetimes of above 300 ps have also been observed in α-FeOOH.[35] Long-living photoinduced polaronic distortions and a negligible contribution from optically-induced thermal displacements have also been reported for lead halide perovskites.[20,36]

The polaron formation time observed by FTAS in the optical range and by pump-probe XANES is evaluated by the analysis of different transitions. In FTAS a swift relaxation of the energy associated with the electrons in photoexcited 4f levels provided the time constant for polaron formation.[14] Pump-probe Ce L_3-edge XAS probes transitions from the 2p core level to the 5d conduction band, which are influenced by transient occupation of the 4f levels and by structural changes induced by the rapid elongation of the oxygen first coordination shell. The quantitative agreement between the characteristic times determined by FTAS and by pump-probe Ce L_3-edge XAS reinforces the correct interpretation of the results obtained by the two methods.

Thermal effects are known to influence the transient response to photoexcitation and can be challenging to distinguish from changes in electronic and structural properties.[37] However, the present study focuses on the structural modifications and electronic relaxation observed within a few hundred femtoseconds after photoexcitation, allowing us to exclude significant thermal effects from influencing the observed polaron formation time. Thermal effects typically become visible a few ps after photoexcitation due to the electron-phonon relaxation timescales and partially contribute only at longer delay times.

The present study provides an important foundation for further research, for example, by assessing the influence of defects with controlled density on the properties and mobility of photoexcited charges at different temperatures, thus aiming at a controlled optimization of this class of photocatalysts.

4. Conclusion

The analysis of pump-probe Ce L_3-edge XANES and EXAFS spectra reveals modifications in both the electronic and local atomic structure of a cerium oxide film following photoexcitation. Within the response time of the experiment (a few tens of femtoseconds), the electronic structure exhibits ultrafast changes consistent with transient occupation of Ce 4f states. This is followed by a partial relaxation into a metastable photoexcited state, characterized by a time constant of 0.45 ps. Concurrently, a structural expansion of ≈0.14 Å occurs in the first shell of oxygen atoms surrounding the excited Ce ion—consistent with values predicted by DFT—indicating the formation of a photoinduced polaronic state. Both the electronic and structural modifications persist for over 300 ps after the photoexcitation.

5. Experimental Section

Experimental Details: The sample for this experiment was a 50 nm thick cerium oxide film, grown by reactive magnetron sputtering using a sapphire disc as a substrate. The pristine substrate was cleaned by immersing it in an acetone bath at 150 °C for 5 min, followed by an ultrasonic bath in acetone and by an ultrasonic bath in isopropanol at 80 °C for 3 min. The cerium oxide film was deposited using a 3″ cerium oxide target in a flux of 20 sccm of an O_2/Ar mixture with 75% O_2, applying a power of 150 W. The substrate temperature was maintained at 300 °C during the growth process to optimize the structure and stoichiometry of the sample. The cerium oxide film thickness was chosen to be 50 nm to match the laser penetration depth at the grazing incidence angle used, thereby maximizing the laser-sample interaction. The film thickness was determined using a quartz microbalance, calibrated by measuring the actual thickness of a cerium oxide film with a profilometer. The preliminary sample characterization, which involved X-ray photoemission spectroscopy, UV–vis spectrophotometry and X-ray diffraction (see Figures S1–S3, Supporting Information, for details), revealed that the sample is polycrystalline, stoichiometric, with the expected fluorite structure and an optical absorption spectrum compatible with the ones observed on CeO_2 films.[14,38]

Two reference samples, in the form of pellets, were also prepared for comparison by mixing cellulose with powdered compounds containing Ce^{4+} (CeO_2) and Ce^{3+} ($Ce(NO_3)_3$-$6H_2O$).

The pump-probe XAS measurements were performed at the FXE instrument of the Eu-XFEL.[22,39] XFEL pulses were delivered in the burst mode, using 40 pulses per pulse-train with an intra-train repetition rate of 141 kHz and 10 trains per second. The two-bounce Si(111) monochromator provided a monochromatic beam with energy resolution $\Delta E/E \sim 10^{-4}$. The photon energy was scanned across the Ce L_3 edge in the 5.7–6.1 keV photon energy range. The changes in the angle of the monochromator across the EXAFS energy range induce slight modifications (≈200 µm) in the travel distance of the X-ray beam modifying the X-ray arrival time at the sample position. To compensate for these changes, the optical delay stage was adjusted accordingly during the scan in the EXAFS energy range. The beam was focused to an average spot size of ≈100 × 100 µm^2 FWHM. The XANES measurements were acquired using a wide area photodiode facing the sample at normal emission. The sample was mounted at a 10° incidence angle – to minimize sample damage – in a chamber fluxed with He and kept at room temperature. The pump pulses, with a wavelength of 267 nm, were synchronized with each alternate train of the XFEL pump. The laser energy per pulse was set to ≈9 µJ pulse^{-1}, that, considering the spot FWHM of 110 × 165 µm^2 gives an incident fluence of 9.4 mJ cm^2. The laser was almost collinear with the XFEL beam at 12.5° incidence angle to minimize the delay time spread.

The damage thresholds for both the laser pump and XFEL beam fluences were determined by comparing steady-state XANES spectra acquired before and after extended exposure at varying fluence levels. For the experiment described here, the laser and XFEL fluences were carefully selected to remain well below the threshold at which detectable modifications occurred. To further minimize beam damage effects, steady-state XANES spectra were measured and compared at regular intervals during extended exposure, approximately after every few hours. Furthermore, to reduce cumulative beam damage, measurements were conducted on a fresh spot of the sample surface approximately every three hours. Particular attention was paid to verifying that, at negative delay times close to zero, the transient spectra remained flat within the noise level.

The XANES and EXAFS spectra were processed using the Demeter software package,[40] including ATHENA, a software for data processing and background subtraction, and ARTEMIS for EXAFS simulation using scattering functions simulated using FEFF.[28] The analysis was limited to the first coordination shell of Ce in CeO_2, consisting of eight oxygen atoms in cubic geometry. The k and R ranges used for fitting were 2–8 Å^{-1} and 1.25–2.35 Å, respectively. The fitting was performed simultaneously on k-, k^2-, and k^3-weighted spectra. Multiple excitations are known to affect the L-edges of rare earths,[41,42] however, in view of the restricted energy range in this analysis, the presence of weak multiple excitation features, due to their expected very low amplitude was neglected.

Computational Details: Constrained Density Functional Theory calculations were performed with the Quantum ESPRESSO software package.[43,44] It was used norm-conserving gauge incuding projector augmented wave pseudopotentials[45] with the following pseudoatomic configurations: O-$2s^2 2p^4$ and Ce-$4f^1 5s^2 5d^1 6s^2$. We have included a Hubbard U-correction with U = 3 eV on the cerium f-orbitals.[29] This value was chosen in such a way as to produce a ground state electronic structure for the pristine CeO_2 unit cell in agreement with existing literature.[12,30–34] Such a value of U also yields a good agreement with previous studies regarding the distorted, constrained state induced by excess charges.[12,30–34]

The pristine CeO_2 fluorite structure was optimized using a 4 × 4 × 4 k-point grid and a wave function cutoff of 150 Ry. The resulting lattice parameter was 5.47 Å in agreement with experimental values within 1%. To model the excited state we have used a 2 × 2 × 2, simple cubic 96-atom supercell, which is known to yield results already close to the thermodynamic limit for electron polaron energies.[32] The reciprocal-space k-point sampling was thus reduced to 2 × 2 × 2 consistently with the pristine case. The calculations were performed at fixed volume, without imposing symmetries to the system and allowing spin polarization. It was calculated i) a pristine supercell (for reference), ii) a supercell with one excess electron added to the Ce-4f band, iii) a supercell with one excess hole added to the O-2p band, iv) a supercell with both an excess electron and an excess hole. In the latter case, the electron-hole pair was constrained in the lowest-energy spin triplet configuration.[46] The structure was optimized in several steps until the total energy was converged below 3 meV, the forces acting on all ions were below 0.5 meV Å^{-1}, considering a convergence threshold for the self-consistency error of 1e-10. In cases ii) and iv), the local octahedral coordination symmetry of oxygens around a chosen cerium atom was initially slightly broken to accelerate convergence to a

lower-energy polaronic state (the same was done around an oxygen site for case iii).

Supporting Information

Supporting Information is available from the Wiley Online Library or from the author.

Acknowledgements

Supported by the Italian Ministry of Foreign Affairs and International Cooperation (MAECI) through the project "Ultrafast Dynamics in Materials for Energy Conversion (U-DYNAMEC)" under the program 2023 Italy – Germany Science and Technology Cooperation. G.A. acknowledges funding from the European Union – NextGenerationEU, M4C2, within the PNRR project NFFA-DI, CUP B53C22004310006, IR0000015. F.P. and D.V. acknowledge Davide Ceresoli for advice on cerium pseudopotentials and self-consistent results for Hubbard parameters in CeO_2. Gianluca Malavasi is acknowledged for providing the Ce^{3+} reference compound. The authors acknowledge European XFEL in Schenefeld, Germany, for provision of X-ray free-electron laser beamtime at FXE under proposal numbers 3435 and 5644 and would like to thank the staff for their assistance.

Conflict of Interest

The authors declare no conflict of interest.

Data Availability Statement

The data that support the findings of this study are openly available in European XFEL at https://doi.org/[10.22003/XFEL.EU-DATA-005644-00], reference number 5644.

Keywords

cerium oxide film, free electron laser, photoinduced polaron, pump probe XAS

Received: June 29, 2025
Revised: August 22, 2025
Published online:

[1] R. Qian, H. Zong, J. Schneider, G. Zhou, T. Zhao, Y. Li, J. Yang, D. W. Bahnemann, J. H. Pan, *Catal. Today* **2019**, *335*, 78.
[2] A.-M. El-Sayed, M. B. Watkins, V. V. Afanas'ev, A. L. Shluger, *Phys. Rev. B* **2014**, *89*, 125201.
[3] C. Franchini, M. Reticcioli, M. Setvin, U. Diebold, *Nat. Rev. Mater.* **2021**, *6*, 560.
[4] M. Barroso, S. R. Pendlebury, A. J. Cowan, J. R. Durrant, *Chem. Sci.* **2013**, *4*, 2724.
[5] J. Husek, A. Cirri, S. Biswas, L. R. Baker, *Chem. Sci.* **2017**, *8*, 8170.
[6] E. Pastor, M. Sachs, S. Selim, J. R. Durrant, A. A. Bakulin, A. Walsh, *Nat. Rev. Mater.* **2022**, *7*, 503.
[7] A. J. Tanner, G. Thornton, *J. Phys. Chem. Lett.* **2022**, *13*, 559.
[8] A. Trovarelli, *Catal. Rev.* **1996**, *38*, 439.
[9] A. Trovarelli; P. Fornasiero, *Catalysis by Ceria and Related Materials*, 2nd ed., Imperial College Pr, London, **2013**.
[10] S. N. Naidi, M. H. Harunsani, A. L. Tan, M. M. Khan, *J. Mater. Chem. B* **2021**, *9*, 5599.
[11] I. K. Naik, T. Y. Tien, *J. Phys. Chem. Solids* **1978**, *39*, 311.
[12] J. J. Plata, A. M. Márquez, J. F. Sanz, *J. Phys. Chem. C* **2013**, *117*, 14502.
[13] D. Zhang, Z.-K. Han, G. E. Murgida, M. V. Ganduglia-Pirovano, Y. Gao, *Phys. Rev. Lett.* **2019**, *122*, 096101.
[14] J. S. Pelli Cresi, L. Di Mario, D. Catone, F. Martelli, A. Paladini, S. Turchini, S. D'Addato, P. Luches, P. O'Keeffe, *J. Phys. Chem. Lett.* **2020**, *11*, 5686.
[15] L. M. Carneiro, S. K. Cushing, C. Liu, Y. Su, P. Yang, A. P. Alivisatos, S. R. Leone, *Nat. Mater.* **2017**, *16*, 819.
[16] A. Koide, Y. Uemura, D. Kido, Y. Wakisaka, S. Takakusagi, B. Ohtani, Y. Niwa, S. Nozawa, K. Ichiyanagi, R. Fukaya, S. Adachi, T. Katayama, T. Togashi, S. Owada, M. Yabashi, Y. Yamamoto, M. Katayama, K. Hatada, T. Yokoyama, K. Asakura, *Phys. Chem. Chem. Phys.* **2020**, *22*, 2615.
[17] D. Kido, Y. Uemura, Y. Wakisaka, A. Koide, H. Uehara, Y. Niwa, S. Nozawa, K. Ichiyanagi, R. Fukaya, S. Adachi, T. Sato, H. Jenkins, T. Yokoyama, S. Takakusagi, J. Hasegawa, K. Asakura, *Chem. Lett.* **2022**, *51*, 1083.
[18] A. Katoch, S. H. Park, K. Jeong, M. Lazemi, R.-P. Wang, H. S. Ahn, T. K. Kim, F. M. F. de Groot, S. Kwon, *Adv. Opt. Mater.* **2024**, *12*, 2401386.
[19] J. S. Pelli Cresi, E. Principi, E. Spurio, D. Catone, P. O'Keeffe, S. Turchini, S. Benedetti, A. Vikatakavi, S. D'Addato, R. Mincigrucci, L. Foglia, G. Kurdi, I. P. Nikolov, G. De Ninno, C. Masciovecchio, S. Nannarone, J. Kopula Kesavan, F. Boscherini, P. Luches, *Nano Lett.* **2021**, *21*, 1729.
[20] O. Cannelli, N. Colonna, M. Puppin, T. C. Rossi, D. Kinschel, L. M. D. Leroy, J. Löffler, J. M. Budarz, A. M. March, G. Doumy, A. Al Haddad, M.-F. Tu, Y. Kumagai, D. Walko, G. Smolentsev, F. Krieg, S. C. Boehme, M. V. Kovalenko, M. Chergui, G. F. Mancini, *J. Am. Chem. Soc.* **2021**, *143*, 9048.
[21] W. Decking, S. Abeghyan, P. Abramian, A. Abramsky, A. Aguirre, C. Albrecht, P. Alou, M. Altarelli, P. Altmann, K. Amyan, V. Anashin, E. Apostolov, K. Appel, D. Auguste, V. Ayvazyan, S. Baark, F. Babies, N. Baboi, P. Bak, V. Balandin, R. Baldinger, B. Baranasic, S. Barbanotti, O. Belikov, V. Belokurov, L. Belova, V. Belyakov, S. Berry, M. Bertucci, B. Beutner, et al., *Nat. Photonics* **2020**, *14*, 391.
[22] A. Galler, W. Gawelda, M. Biednov, C. Bomer, A. Britz, S. Brockhauser, T.-K. Choi, M. Diez, P. Frankenberger, M. French, D. Gorries, M. Hart, S. Hauf, D. Khakhulin, M. Knoll, T. Korsch, K. Kubicek, M. Kuster, P. Lang, F. Alves Lima, F. Otte, S. Schulz, P. Zalden, C. Bressler, *J. Synchrotron Radiat.* **2019**, *26*, 1432.
[23] P. Luches, F. Pagliuca, S. Valeri, F. Boscherini, *J. Phys. Chem. C* **2013**, *117*, 1030.
[24] D.-C. Sergentu, C. H. Booth, J. Autschbach, *Chem. – A Eur. J.* **2021**, *27*, 7239.
[25] K. O. Kvashnina, S. M. Butorin, P. Glatzel, *J. Anal. At. Spectrom.* **2011**, *26*, 1265.
[26] G. Gasperi, L. Amidani, F. Benedetti, F. Boscherini, P. Glatzel, S. Valeri, P. Luches, *Phys. Chem. Chem. Phys.* **2016**, *18*, 20511.
[27] W. Gawelda, V. T. Pham, R. M. van der Veen, D. Grolimund, R. Abela, M. Chergui, C. Bressler, *J. Chem. Phys.* **2009**, *130*, 124520.
[28] M. Newville, *J. Synchrotron Radiat.* **2001**, *8*, 322.
[29] S. L. Dudarev, G. A. Botton, S. Y. Savrasov, C. J. Humphreys, A. P. Sutton, *Phys. Rev. B* **1998**, *57*, 1505.
[30] C. Loschen, J. Carrasco, K. M. Neyman, F. Illas, *Phys. Rev. B* **2007**, *75*, 035115.
[31] L. Sun, X. Huang, L. Wang, A. Janotti, *Phys. Rev. B* **2017**, *95*, 245101.
[32] C. W. M. Castleton, A. Lee, J. Kullgren, *J. Phys. Chem. C* **2019**, *123*, 5164.
[33] M. Nakayama, H. Ohshima, M. Nogami, M. Martin, *Phys. Chem. Chem. Phys.* **2012**, *14*, 6079.
[34] T. Zacherle, A. Schriever, R. A. De Souza, M. Martin, *Phys. Rev. B* **2013**, *87*, 134104.

[35] I. J. P. Molesky, S. K. Cushing, L. M. Carneiro, A. Lee, J. C. Ondry, J. C. Dahl, H.-T. Chang, A. P. Alivisatos, S. R. Leone, *J. Phys. Chem. Lett.* **2018**, *9*, 4120.
[36] M. Park, A. J. Neukirch, S. E. Reyes-Lillo, M. Lai, S. R. Ellis, D. Dietze, J. B. Neaton, P. Yang, S. Tretiak, R. A. Mathies, *Nat. Commun.* **2018**, *9*, 2525.
[37] L. Wang, R. Nughays, T. C. Rossi, M. Oppermann, W. Ogieglo, T. Bian, C.-H. Shih, T.-F. Guo, I. Pinnau, J. Yin, O. M. Bakr, O. F. Mohammed, M. Chergui, *J. Am. Chem. Soc.* **2024**, *146*, 5393.
[38] E. Spurio, J. S. Pelli Cresi, G. Ammirati, S. Pelatti, A. Paladini, S. D'Addato, S. Turchini, P. O'Keeffe, D. Catone, P. Luches, *ACS Photonics* **2023**, *10*, 1566.
[39] D. Khakhulin, F. Otte, M. Biednov, C. Bömer, T.-K. Choi, M. Diez, A. Galler, Y. Jiang, K. Kubicek, F. A. Lima, A. Rodriguez-Fernandez, P. Zalden, W. Gawelda, C. Bressler, *Appl. Sci.* **2020**, *10*, 995.
[40] B. Ravel, M. Newville, A. Athena, *J. Synchrotron Radiat.* **2005**, *12*, 537.
[41] J. A. Solera, J. García, M. G. Proietti, *Phys. Rev. B* **1995**, *51*, 2678.
[42] E. Fonda, D. Andreatta, P. E. Colavita, G. Vlaic, *J. Synchrotron Radiat.* **1999**, *6*, 34.
[43] P. Giannozzi, O. Andreussi, T. Brumme, O. Bunau, M. Buongiorno Nardelli, M. Calandra, R. Car, C. Cavazzoni, D. Ceresoli, M. Cococcioni, N. Colonna, I. Carnimeo, A. Dal Corso, S. de Gironcoli, P. Delugas, R. A. DiStasio, A. Ferretti, A. Floris, G. Fratesi, G. Fugallo, R. Gebauer, U. Gerstmann, F. Giustino, T. Gorni, J. Jia, M. Kawamura, H. Y. Ko, A. Kokalj, E. Küçükbenli, M. Lazzeri, et al., *J. Phys.: Condens. Matter* **2017**, *29*, 465901.
[44] P. Giannozzi, O. Baseggio, P. Bonfà, D. Brunato, R. Car, I. Carnimeo, C. Cavazzoni, S. de Gironcoli, P. Delugas, F. Ferrari Ruffino, A. Ferretti, N. Marzari, I. Timrov, A. Urru, S. Baroni, *J. Chem. Phys.* **2020**, *152*, 154105.
[45] C. Tantardini, A. G. Kvashnin, D. Ceresoli, *Materials* **2022**, *15*, 3347.
[46] C. Di Valentin, A. Selloni, *J. Phys. Chem. Lett.* **2011**, *2*, 2223.